Prediction of Mobility and Burial of Objects on Sandy Seafloor

Peter C. Chu, Chenwu Fan, Joseph Calantoni, *Member, IEEE*, and Alex Sheremet

***Abstract*—A numerical model was developed to predict mobility and burial of seafloor cylindrical objects. The model contains four components: 1) object's physical parameters such as diameter, length, mass, and rolling moment; 2) dynamics of rolling cylinder around its major axis; 3) empirical sediment scour model; and 4) seabed environmental characteristics such as currents, waves (peak period, significant wave height), sediment density, and medium sediment grain size. Under the sponsorship of the Department of Defense Strategic Environmental Research and Development Program, a field experiment was conducted from April 21 to May 23, 2013 off the coast of Panama City, FL, USA to measure both objects' mobility using sector scanning and pencil beam sonars and simultaneous environmental time-series data of the boundary layer hydrodynamics and sediment transport conditions for driving mobility. Comparison between modeled and observed data shows the model capability. Future work needs to consider more realistic object shapes and motions such as pitch and yaw, and wavy seabed.**

***Index Terms*—Equilibrium burial percentage, munitions mobility and burial, object mobility model, object shields parameter, sediment shields parameter, sediment supporting point.**

NOMENCLATURE

(a_1, a_2, a_3)	Empirical coefficients (25).
B	Object burial depth (m) [(8), (11), (12), (14), (15a), (17), (28)].
b	Depth of rotation axis in sediment (m) [(2), (8), (11), (14), (15a), (17)].
(c_1, c_2)	Coefficients in e-folding time scale for scour burial [see (27)].
(C_d, C_l)	(Drag, Lift) Coefficients [(12), (13)].
D	Diameter of cylindrical object (m) [(2), (7), (8), (12), (14), (15a), (17), (18), (21), (27), (28)].
d_{50}	Medium of the grain diameter (m) [(1), (24), (27)].
$(\mathbf{e}_h, \mathbf{e}_v)$	Horizontal and vertical unit vectors [(4), (5)].
f	Wave friction factor [see (24)].
F_a	Added mass (N) [(12), (14)].
F_d	Water drag force (N) [(12), (14)].
F_l	Water lift force (N) [(12), (14)].
F_w	Buoyancy force (N) [(12), (14)].
h	Mean water level (m).
H_S	Significant wave height (m).
I_A	Rolling moment of object about b without added mass (kg m^2) [(16), (17), (18)].
I_A^*	Rolling moment of object about b with added mass (kg m^2) [see (17)].
I_o	Rolling moment of object about its symmetric axis (kg m^2) [see (18)].
L	Length of cylindrical object (m) [(12), (21)].
l	Displacement of object (m) [see (23)].
M	Mass of object (kg).
$\mathbf{n}$	Unit vector normal to the cylinder surface [(3), (4)].
p_B	Object percentage burial [(15a), (16), (17), (20), (21), (22), (26), (28)].
$p_{B,\mathrm{eq}}$	Equilibrium percentage burial [(25), (26)].
p_b	Relative depth of rotation axis in sediment [(15a), (21), (28)].
S_o	Relative object's density versus water density [(15a), (21)].
S_{sed}	Relative sediment's density versus water density [see (24)].
$T*$	e-Folding time scale for reaching equilibrium scour burial (s) [(26), (27)].
T_B	Torque to roll the object backward (N m) [see (16)].
T_F	Torque to roll the object forward (N m) [(16), (17)].
T_P	Wave peak period (s) [see (24)].
$\mathbf{T}_S$	Sediment torque on object (N m) [(6), (9)].
U_c	Bottom current speed (m·s^{-1}).
U_{br}	Bottom wave orbital velocity (m·s^{-1}) [see (24)].
u_o	Object's rolling horizontal velocity (m·s^{-1}) [(2), (3), (5), (19), (23)].
$\hat{u}_o$	Relative object's rolling horizontal velocity [(19), (20), (22)].
U	Component of $\mathbf{V}_w$ perpendicular to the object's main axis (m·s^{-1}) [(12), (15a), (21)].

Manuscript received August 5, 2020; revised April 12, 2021 and June 19, 2021; accepted July 12, 2021. Date of publication September 29, 2021; date of current version January 13, 2022. The work of Peter C. Chu and Chenwu Fan was supported by the SERDP Munition Response Program through Project MR-19-1073 titled "Coupled Ensemble Sea-Floor Environment and 6-DOF (CESE6D) Model for Assessing Characteristics of Munitions Underwater and Their Environment." The work of Joseph Calantoni was supported by the SERDP Munition Response Program through Project MR-2320 titled "Long Time Series Measurements of Munitions Mobility in the Wave-Current Boundary Layer." *(Corresponding author: Peter C. Chu.)*

Associate Editor: N. Chotiros.

Peter C. Chu and Chenwu Fan are with the Naval Ocean Analysis and Prediction Laboratory, Department of Oceanography, Naval Postgraduate School, Monterey, CA 93943 USA (e-mail: pcchu@nps.edu; chenwu.fan.ctr@nps.edu).

Joseph Calantoni is with Ocean Sciences Division, U.S. Naval Research Laboratory, Stennis Space Center, Bay Saint Louis, MS 39529 USA (e-mail: joe.calantoni@nrlssc.navy.mil).

Alex Sheremet is with the Engineering School of Sustainable Infrastructure and Environment, University of Florida, Gainesville, FL 32611 USA (e-mail: alex@coastal.ufl.edu).

Digital Object Identifier 10.1109/JOE.2021.3098391

V	Components of $\mathbf{V}_w$ parallel to the object's main axis ($\mathrm{m{\cdot}s^{-1}}$).
$\mathbf{V}_w$	Bottom water velocity (current and wave) vector ($\mathrm{m{\cdot}s^{-1}}$).
(v_e, v_n)	Bottom current velocity vector ($\mathrm{m{\cdot}s^{-1}}$).
w	Weight coefficient for unburial parameterization [see (29)].
(α, β)	Coefficients in the object mobility model [(20), (21), (22)].
γ	Ratio of lift versus drag coefficient [(13), (15a)].
θ_{opb}	Object burial percentage Shields parameter [(15a), (15b), (16), (17), (20), (22)].
θ_{sed}	Sediment Shields parameter [(24), (25), (27)].
λ	Ratio between b and B [(11), (28)].
Π	Volume of object ($\mathrm{m^3}$) [(17), (18), (21)].
ρ_o	Density of object ($\mathrm{kg{\cdot}m^{-3}}$) [(15a), (17), (18)].
ρ_s	Density of sediment ($\mathrm{kg{\cdot}m^{-3}}$) [see (24)].
ρ_w	Density of seawater ($\mathrm{kg{\cdot}m^{-3}}$) [(12), (17), (21), (24)].
ψ	Radial angle around the center of cylinder from the vertical axis.
ω	Angular velocity of rolling object ($\mathrm{s^{-1}}$) [(2), (16), (17)].

I. Introduction

PREDICTION of the mobility and burial of a rigid object on the seafloor is confounded by the influence of environmental characteristics such as waves, currents, sediment dynamics, and seafloor morphology. The phenomenology of munitions, mines, and other objects in shallow underwater environments has broad military and civilian applications. For example, formerly used Defense sites have vast underwater environments that are contaminated with munitions and other unexploded ordnance that need to be managed and remediated [1].

We expect similarities exist between the prediction of burial and mobility for both underwater munitions and sea mines. Observations show that mine burial is sensitive to the sediment type, hydrodynamic forcing, and the size and shape of the mine [2]. A physical model to predict mobility and burial of an object on the seafloor has six degrees of freedom (DoF), and is usually called a 6-DoF model [3]. Three degrees of freedom refer to the position of center of mass of the object, and the other three degrees of freedom represent the orientation of the object (i.e., roll, yaw, and pitch). The 6-DoF model is based on the approach previously developed to predict sea mine impact burial, named IMPACT35, which predicts the trajectory of a mine through air and water, in addition to the amount of burial that occurs upon impact with the seafloor [4]–[6]. The IMPACT35 model contains full physics including nonlinear dynamics, fluid-structure interaction, instability theory [7], and bearing factor method to calculate the sediment force and torque with cavities for mine movements in sediment [8]. We have modified the existing 6-DoF model (IMPACT35) to predict the burial and mobility of idealized munitions (i.e., cylindrical objects) on the seafloor. Previous experimental observations [9]–[11] and statistical modeling [12] focus on the determination of the conditions that initiate motion, specifically, the roll of a munition around its principle axis, both on a hard surface and on a sand bed in the presence of concurrent scour burial. Mobility of an object on the seafloor is characterized by the balance between the destabilizing hydrodynamics and the stabilizing weight of the object [13], [14]. The Shields parameter for object percentage burial θ_{opb} is estimated using the size and density of the object as well as the local velocity perpendicular to its main axis, U. The critical value for the mobility threshold of cylindrical objects was found to occur for, $\theta_{\mathrm{opb}} > 1$.

In noncohesive sandy sediments, objects on the seafloor are subject to scour, which is a common burial mechanism that is controlled by the fluid velocity relative to other environmental characteristics of the sediments, regional pressure gradients, tidal forcing, and the orbital velocity of waves. The nondimensional sediment Shields parameter θ_{sed} is important for the scour burial. The existing experimental observations and statistical modeling [9]–[14] provide a useful framework for the development of a model for munitions.

A model to predict objects' mobility and burial on sandy seafloor has been developed in this study based on the following four assumptions:

1) cylindrical munition with a large aspect ratio (length L much larger than diameter D, $L>>D$);
2) roll dominating the motion of the long cylinder ($L >> D$) with no yaw and pitch;
3) burial depth (B) smaller than half of the diameter ($B < D/2$) [10];
4) flat seabed.

Fig. 1 shows the flowchart of this prediction system. It consists of four parts:

1) cylindrical object model with the burial percentage Shields parameter (θ_{opb});
2) sediment scour model with sediment Shields parameter (θ_{sed});
3) input data such as object's physical parameters (D, S_o, M, I_o), and environmental variables such as near seabed ocean currents, bottom wave orbital velocity (U_{br}) water depth (h), wave peak period (T_P), significant wave height (H_S), sediment characteristics;
4) model output such as the burial percentage p_B, and the object's displacement.

The rest of the article is outlined as follows. Section II describes the experimental design and methods. Section III presents the results of sedimentology and hydrodynamic observations from the field experiment. Section IV presents the sediment supporting point for estimating rolling motion. Section V defines the drag, lift, buoyancy forces, and added mass. Section VI presents the object mobility prediction model. Section VII presents the scour burial model. Section VIII shows the comparison between the field observations and model prediction of objects' mobility and burial. Finally, Section IX concludes this article.

II. Field Experiment

A field experiment was conducted from April 21, 2013 to May 23, 2013 to monitor the waves and currents as well as to simultaneously track the location of surrogate munitions on the seafloor [9]. The combined observations of munitions mobility

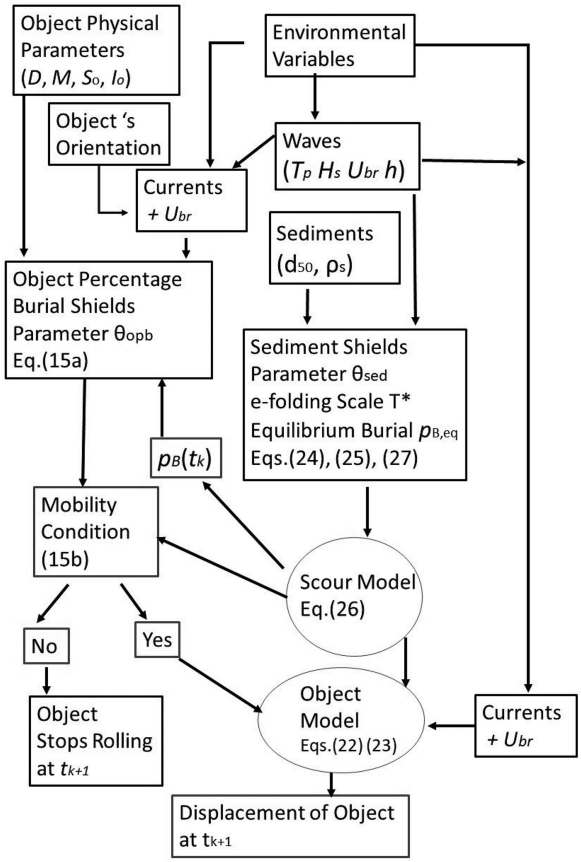

Fig. 1. Flowchart of the prediction system for objects' mobility and burial. See the nomenclature list and text for definitions and derivations of parameters.

and the driving hydrodynamic conditions provide data for model development to predict seafloor munitions' mobility and burial. During the field experiment, a range of surrogate munitions were deployed that include variations in caliber, bulk density, shape, and rolling moment.

A. Surrogate Munitions

Four types of surrogate and replica munitions that roughly represented the 155-mm HE M107, 81-mm mortar, 25-mm cartridge, and 20-mm cartridge were designed and fabricated using crude drawings and specifications provided by existing Army Technical Manuals (e.g., TM 43-0001-27 and TM 43-0001-28). Additional replica munitions for each of the four types listed above were purchased commercially. The purchased replicas were used to provide overall dimensions and shape details for the four types of munitions. These purchased replicas were constructed from solid urethane casts for the 155- and 81-mm calibers and solid aluminum for the 25- and 20-mm calibers (note the purchased 155-mm caliber was positively buoyant and not deployed).

A total of four surrogate munitions and nine replicas were deployed at each of two water depths adjacent to the quadpod instrument frames (described later). Replica munitions have the general dimensions and shape of their real counterparts; however, replica munitions are constructed from a single solid material to cover a range of munitions' bulk density. Surrogate munitions are similar in size and shape to replicas except they were fabricated to have bulk densities and rolling moments that more closely match their real counterparts. The complete list of deployed and recovered objects along with brief descriptions and their material properties is given in Table I. The mass for each object was determined post fabrication before deployment. The density listed for the replicas fabricated from a single solid material is the known material density. The volume and rolling moments for all objects were estimated using CAD software. For the surrogates and replicas that are composites of more than one material the bulk density was estimated by combining the measured mass and the volume estimate from the CAD software. Photographs for the four types of surrogate munitions are shown in Fig. 2. The first type was designed to represent the projectile, 155 mm, HE, M107, typically fired from 155-mm howitzers [Fig. 2(a)]. The second type was designed to represent the 81-mm mortar [Fig. 2(b)]. The third and fourth types were designed to represent the cartridges, 25 and 20 mm [Fig. 2(c)]. Each of the photographs contains the fabricated surrogate, the purchased replica, and the replica fabricated from a single solid piece of aluminum [for 155 mm; see Fig. 2(a) bottom], with a solid stainless-steel body and aluminum tail section [for 81 mm; see Fig. 2(b) bottom], with a steel projectile fabricated with nearly identical density and dimensions to those found in the Army Technical Manual [for 25- and 20-mm cartridges; see Fig. 2(c) bottom].

Rolling moment for each surrogate or replica is also measured since it is an important parameter for the mobility. The difference in rolling moment calculated for the 81-mm surrogate with and without fins is only 4.4%. While the fins seemingly add little to the total rolling moment, their interaction with the seafloor and bottom currents should not be underestimated. For 25- and 20-mm cartridges, a solid piece of Delrin plastic cut in the shape of the shell casing very closely matches the weight of the remaining portion of the munitions. Note that while a steel projectile is very common for the 20-mm type, we realize that the projectiles for the 25-mm type may be much more sophisticated and varied. Here, we assumed the simplest solid steel projectile for the 25-mm type.

B. Instrumentation and Deployment

Instruments to observe the local hydrodynamics and resulting munitions' mobility were mounted on a pair of large rugged frames (herein referred to as "quadpods") that were deployed at two different water depths (herein referred to as "deep" and "shallow") during the Target and Reverberation Experiment (TREX13). The quadpods were deployed in the northern Gulf of Mexico offshore Panama City Beach, FL, USA [see Fig. 3(a)]. The deep quadpod was deployed at 30° 03.02330 N, 85° 41.33630 W, in about 20-m water depth, whereas the shallow quadpod was deployed at 30° 04.80994 N, 85° 40.41064 W, in about 7.5-m water depth. Fig. 3(b) shows the deployment of the quadpod from a research ship.

TABLE I
LIST OF SURROGATE AND REPLICA MUNITIONS USED DURING TREX13

Type with Diameter	**Labels**	***Materials* Type**	**Recovered**	**Rolling Moment** (10^{-4} kg m^2)	**Volume** (10^{-5} m^3)	**Mass** (kg)	**Density** (kg m^{-3})
155 mm, HE, M107	D5, D6	*Delrin, 304 Stainless* Surrogate	D5, D6	923.59	768.38	34.15	4,444
	D3, D4	*Aluminum* Replica	D3, D4	500.48	768.38	20.91	2,721
81 mm mortar	C3, C4	*Delrin, 316 Stainless, Aluminum tail fins* Surrogate	C3, C4	24.73	120.93	3.76	3,109
	C5, C6	*304 Stainless, Aluminum tail fins* Replica	C5, C6	50.51	120.93	8.70	7,194
	C1, C2	*Urethane* Replica		8.34	120.93	1.45	1,199
25 mm cartridge	B5, B6	*Delrin, 316 Stainless* Surrogate	B5, B6	0.46	16.55	0.39	2,356
	B7, B8	*304 Stainless* Replica	B7, B8	1.98	16.55	1.32	7,975
	B3, B4	*Aluminum* Replica	B3, B4	0.68	16.55	0.43	2,598
	B1, B2	*Delrin* Replica		0.35	16.55	0.23	1,390
20 mm cartridge	A5, A6	*Delrin, 316 Stainless* Surrogate	A6	0.13	7.70	0.20	2,597
	A7, A8	*304 Stainless* Replica	A7	0.53	7.70	0.63	8,181
	A3, A4	*Aluminum* Replica	A3, A4	0.18	7.70	0.19	2,468
	A1, A2	*Delrin* Replica		0.09	7.70	0.11	1,429

A total of 26 objects were deployed and 18 objects were recovered (from [9]). Type surrogate munitions were fabricated to have rolling moments within 10% of the estimated rolling moment of the real counterpart.

Waves and currents were obtained using both an acoustical surface tracking (Nortek AWAC) and pressure time series. A sector scanning sonar was mounted on one of the legs of each of the quadpods, scanning a 110° swath every 12 min. The surrogate and replica munitions (described above) were deployed within the view field of the sector scanning sonar. Divers laid the surrogate and replica munitions on the seafloor around each quadpods according to a predetermined schematic. Only objects laid by divers under the shallow quadpod were photographed [see Fig. 4(a)]. The light blue arc roughly denotes the field of view of the sector scanning sonar. The dark blue circle in the upper left denotes the location of the surrogates. The other replicas were grouped according to relative bulk density. In this case, the red boxes denote the objects that were not recovered from the shallow quadpod site. A maintenance dive was performed on the morning of May 8, 2013 immediately after the storm event and found a single clue that the surrogates and replicas may have been buried in place as opposed to being transported away by the waves and currents [see Fig. 4(b)]. The 155-mm replica fabricated from solid aluminum was partially buried in the crest of a sand ripple (see Fig. 5). The sharp crest of the ripple (or bedform) is visible in the foreground of the image, indicated by the black arrow. The replica shown here was the only object not completely buried during the storm event at the shallow quadpod location (see Fig. 5). Excavating by hand, divers were able to recover a total of eight munitions buried just below the surface very near the known initial locations at the shallow quadpod during the maintenance dive performed on May 8, 2013.

III. OBSERVATIONAL DATA

A. Sedimentology

Sediment samples were collected at both shallow and deep quadpod locations during the deployment and retrieval. Two

(a) (b) (c)

Fig. 2. Fabricated surrogate, purchased replica, and fabricated replica of (a) 155-mm HE M107; (b) 81-mm mortar; and (c) 25- and 20-mm cartridges (from [9]).

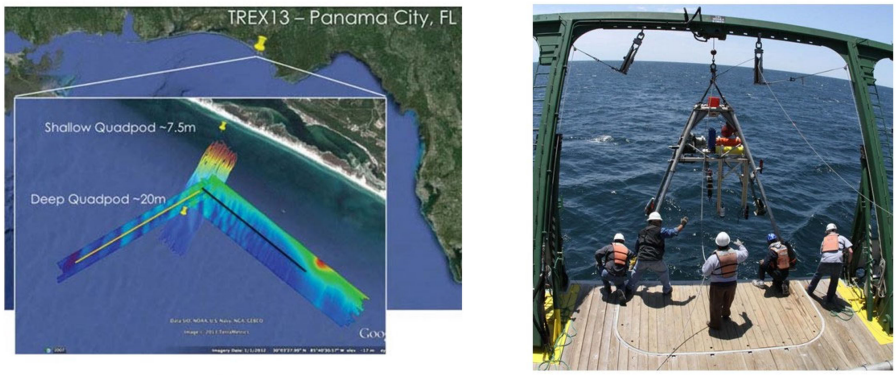

(a) (b)

Fig. 3. (a) Deployment of the deep quadpod with near 3.3-m height into around 20-m depth through the A-frame of *R/V Smith* around 1240 local time on April 20, 2013; and (b) locations of deep and shallow quadpods (from [9]).

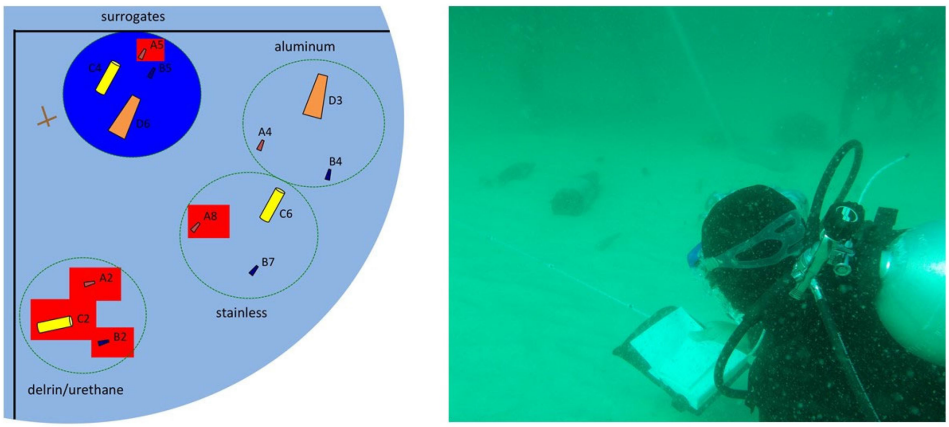

(a) (b)

Fig. 4. (a) Layout of objects laid by divers under the shallow quadpod; and (b) the photograph of divers laying the object field during the shallow quadpod deployment (from [9]).

cores collected at shallow quadpod location have been found to contain nearly 100% sand. Grain size distributions were obtained with standard sieve techniques and results for porosity, bulk density, and void ratio were obtained by measuring the weight loss or water weight. We estimated the median grain diameter (d_{50}) and sediment density (ρ_s) in the upper 6 cm of the bed to be

$$d_{50} = 0.23 \times 10^{-3}\,\text{m}, \qquad \rho_s = 2.69 \times 10^{3}\,\text{kg} \cdot \text{m}^{-3}. \quad (1)$$

B. Waves and Currents

Since no similar initial objects' locations were given for the deep quadpod, we restrict our wave and current data depiction on the shallow quadpod. The waves were observed locally using the acoustical surface tracking of the Nortek AWAC with a frequency of 1 MHz installed at top of shallow and deep quadpods (one for each) from April 21, 2013 to May 23, 2013. The AWAC was placed as 2.3-m height above the bed on the shallow quadpod. Within every 30 min, the AWAC measures

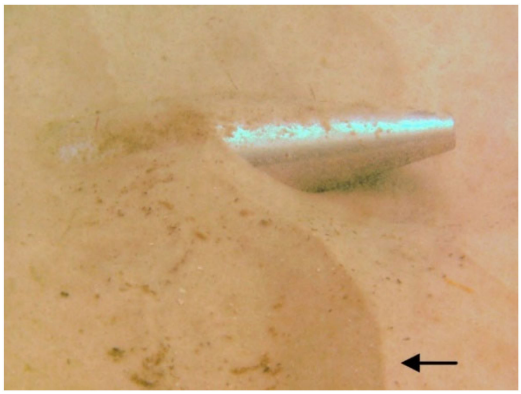

Fig. 5. Object field of the shallow quadpod taken on the morning of May 8, 2013 (from [9]).

high frequency (2 Hz) horizontal water velocity for 20 min. For 20 min starting at the beginning and midpoint of every hour, we obtain the wave statistical analysis to get peak period (T_P), significant wave height (H_S), and mean water level (h). The bottom wave orbital velocity (U_{br}) is the result of interactions between surface waves and the seafloor. A well-established linear wave model with MATLAB function [15] is used to calculate the bottom orbital velocity U_{br} with the water depth (h), significant wave height (H_S), and peak period (T_p) as input and the bottom orbital velocity (U_{br}) as output (see [15, App. D]).

The AWAC was installed at the shallow quadpod with the vertical distance of 0.5 m for two consecutive bins to obtain the current profile vector $\mathbf{U}_c = \mathbf{i}v_e + \mathbf{j}v_n$, with the temporal resolution of 1 min. Here, ($\mathbf{i}$, $\mathbf{j}$) are unit vectors in longitudinal and latitudinal directions. Let $U_c = \sqrt{v_e^2 + v_n^2}$ be the current speed. The currents at the lowest bin (2.3 m above the seabed) were directly taken for forcing surrogates or replicas with diameters around 0.15 m without using the log profile because 2.3 m is far above the seabed log layer. The bottom water velocity vector of combined current and waves is represented by $\mathbf{V}_w$ with $|\mathbf{V}_w| = U_c + U_{br}$ and the orientation $\psi = \tan^{-1}(v_n/v_e)$. Fig. 6 shows the time series of the environmental parameters [v_e, v_n, U_c, h, T_P, H_S, U_{br}]. Two consecutive atmospheric cold fronts passed by the area between May 5 and 7, 2013. The current speed U_c fluctuates from 0 to 0.5 m/s [see Fig. 6(c)] with no evident strengthening during the storm event. The bottom wave orbital velocity (U_{br}) was strengthed drastically from 0.2 m/s before the storm to 0.8 m/s on May 5, 2013 during the storm, and reduced to less than 0.2 m/s after the storm event on May 7, 2013 [see Fig. 6(g)].

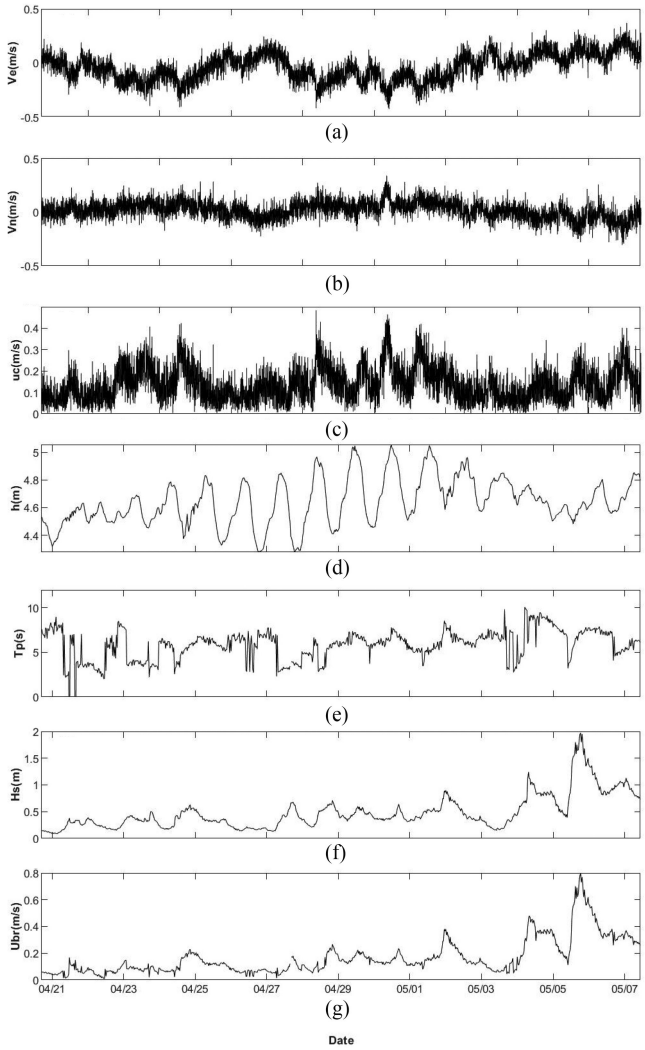

Fig. 6. Time series with 30-min increment of (a) near bed (∼0.15 m) longitudinal current v_e (m/s); (b) near bed (∼0.15 m) latitudinal current v_n (m/s); (c) near bed (∼0.15 m) current speed U_c; (d) water depth h (m) (mean water level plus quadpod's height, 2.3 m); (e) peak period T_P (s), (f) significant wave height H_S (m); and (g) computed bottom wave orbital velocity U_{br} (m/s), at the shallow quadpod from April 21 to May 23, 2013.

IV. Sediment Supporting Point

Roll of an object on the sandy floor needs a supporting point in sediment. Let the water velocity (consisting of current and waves) near the seabed ($\mathbf{V}_w$) be in the direction toward the cylinder with an angle ϕ perpendicular to the main axis of the cylinder, and be decomposed into $\mathbf{V}_w = (U, V)$ with U the perpendicular component, and V the parallel component (see Fig. 7) to the main axis of the cylinder.

As the object rolls with angular velocity ω, let the axis of rotation inside the sediment be at depth b ($b < B$) and let ψ be the radial angle of the cylinder from the vertical axis with ψ_B at the top of sediment, and ψ_b at the depth b (see Fig. 8). The horizontal velocity of the object rolling around the point b is given by

$$u_o = \omega \left(\frac{D}{2} - b \right) \tag{2}$$

with the radial component of $u_o \sin\psi$ at any depth inside the sediment. Thus, the compressive normal stress of sediment on the object is represented by

$$\mathbf{F}_S = -\mathbf{n}\kappa u_o \sin\psi \tag{3}$$

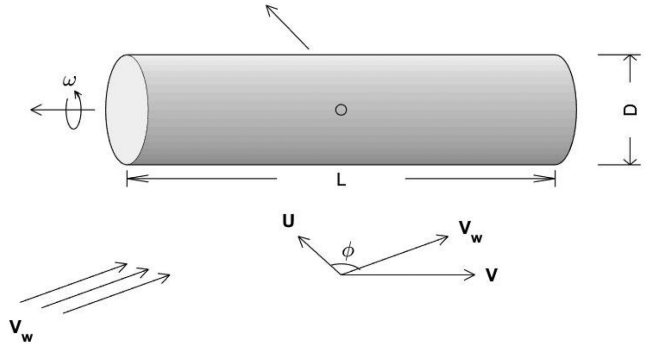

Fig. 7. Roll of a cylindrical object on the seafloor with a large aspect ratio forced by the combination of ocean currents and bottom wave orbital velocity. Here, (π/2–ϕ) is the angle between $\mathbf{V}_w$ and the main axis of the cylinder.

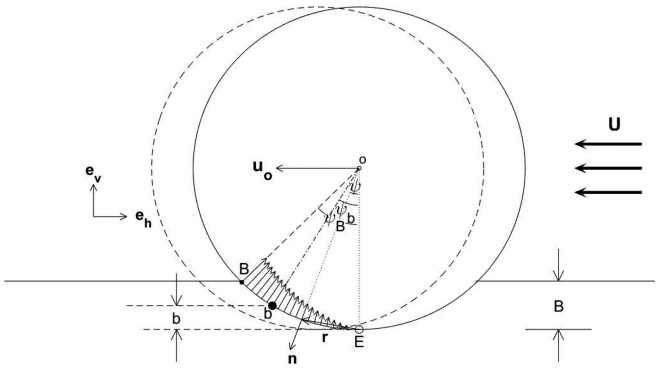

Fig. 8. Location of the axis of rotation of the cylinder in the sediment b is determined by the assumption of zero-sum torque to the roll.

where $\mathbf{n}$ is the unit vector normal to the cylinder surface, and κ is the compressive coefficient. Let $\mathbf{n}$ be decomposed into

$$\mathbf{n} = -\mathbf{e}_h \sin\psi - \mathbf{e}_v \cos\psi \tag{4}$$

where ($\mathbf{e}_h$, $\mathbf{e}_v$) are horizontal and vertical unit vectors (see Fig. 2). The sediment compressive normal stress $\mathbf{F}_S$ is decomposed as

$$\mathbf{F}_S = \mathbf{e}_h \kappa u_o \sin^2\psi + \mathbf{e}_v \kappa u_o \sin\psi\cos\psi. \tag{5}$$

With b as the axis of rotation, the sediment above (below) the depth b generates torque to resist (enhance) the rolling with the total torque from the sediment

$$\begin{aligned}\mathbf{T}_S &= \int_0^{\psi_B} [(\mathbf{r}-\mathbf{r}_b)\times\mathbf{F}_S]d\psi \\ &= \int_0^{\psi_B} [\mathbf{r}\times\mathbf{F}_S]d\psi - \mathbf{r}_b \times \int_0^{\psi_B} \mathbf{F}_S d\psi \end{aligned} \tag{6}$$

where $\mathbf{r}$ is the position vector at any point on the circle and $\mathbf{r}_b$ is the position vector at point b with point E as the origin

$$\begin{aligned}\mathbf{r} &= \frac{D}{2}(-\mathbf{e}_h \sin\psi + \mathbf{e}_v(1-\cos\psi) \\ \mathbf{r}_b &= \frac{D}{2}\left[-\mathbf{e}_h \sin\psi_b + \mathbf{e}_v(1-\cos\psi_b)\right]. \end{aligned} \tag{7}$$

The depths B and b are represented by

$$B = \frac{D}{2}(1-\cos\psi_B), \qquad b = \frac{D}{2}(1-\cos\psi_b). \tag{8}$$

If we assume that at the depth b the total torque from the sediment is zero (i.e., zero-sum sediment torque for rolling), then we have

$$\mathbf{T}_S = 0. \tag{9}$$

Substitution of (5)–(7) into (9) gives

$$\psi_b = \tan^{-1}\left(\frac{\psi_B - \sin\psi_B\cos\psi_B}{\sin^2\psi_B}\right). \tag{10}$$

The ratio $\lambda = b/B$ can be obtained from (8) and (10)

$$\lambda \equiv b/B = \frac{1-\cos\left[\tan^{-1}\left(\dfrac{\psi_B - \sin\psi_B\cos\psi_B}{\sin^2\psi_B}\right)\right]}{1-\cos\psi_B}. \tag{11}$$

The ratio λ varies with the burial percentage $p_B = B/D$ mildly from near 0.4445 for $p_B = 0$ and 0.4630. Here, we take $\lambda = 0.453$ in this study.

V. Drag, Lift, Buoyancy Forces, and Added Mass

The drag force (F_d), lift force (F_l), buoyancy force (F_w), and added mass (F_a) exerted on the object for rolling by the perpendicular component U are given by vv

$$\begin{aligned} F_d &= \frac{\rho_w C_d U^2 L(D-B)}{2}, \qquad F_l = \frac{\rho_w C_l U^2 LD}{2} \\ F_w &= g(\rho_o - \rho_w)\Pi, \qquad F_a = -\rho_w \Pi \frac{du_o}{dt} \end{aligned} \tag{12}$$

where $g = 9.81$ m/s^2 is the gravitational acceleration; $\rho_w = 1025$ kg/m^3 is the density of seawater; ρ_o is the density of the cylindrical object; (C_d, C_l) are the drag and lift coefficients across cylinder's main axis with vortex shedding caused by the oscillating flow (U) due to waves. If time averaged U within a certain time period being used, the mean coefficients for drag and lift (C_d, C_l), depending solely on the Reynolds number and aspect ratio (see Appendix A), can be used. Since the wave component, i.e., the bottom wave orbital velocity in $\mathbf{V}_w$ for the object model is computed from a linear wave model with the temporal resolution of 30 min, the mean coefficients for drag and lift are used. The vortex shedding from objects is neglected. Besides, the lift coefficient is less certain, we assume

$$C_l = \gamma C_d \tag{13}$$

where γ is the ratio of lift coefficient versus drag coefficient with γ being taken as value of 0.2.

The drag force rolls the cylinder forward around the axis of rotation b with the torque per unit length of $F_d(D/2 + B/2 - b)$. Here, B/2 is the distance between the volume center of the cylinder above the sediment (i.e., point C in Fig. 9) and the volume center of the whole cylinder (i.e., point O in Fig. 9). Note that point C is the center of the resultant drag force on the cylinder. The buoyancy force minus lift force resists the cylinder rolling forward caused by the drag with the torque per unit length of $F_w\sqrt{b(D-b)}$ (buoyancy force), $F_l\sqrt{b(D-b)}$

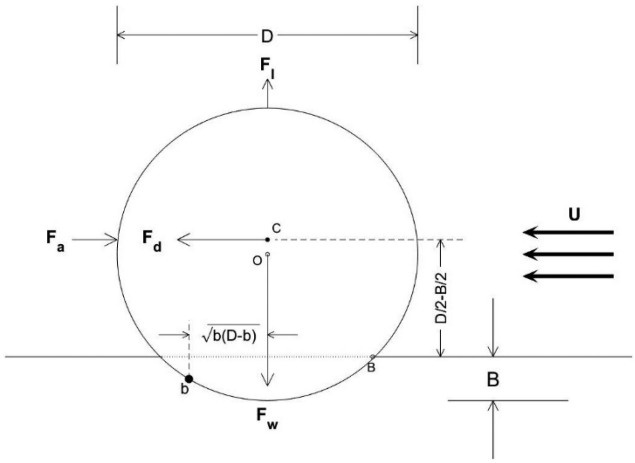

Fig. 9. Forces and torques due to drag, lift, buoyancy, and added mass on a partially buried cylinder by the combination of ocean currents and bottom wave orbital velocity (U) perpendicular to the major axis of the cylinder.

(lift), and the added mass $F_a(D/2+B/2-b)$. The threshold for the mobility of the object is represented by

$$F_d\left(D/2+B/2-b\right)+F_l\sqrt{b\left(D-b\right)} > F_w\sqrt{b\left(D-b\right)}+F_a\left(D/2+B/2-b\right) \tag{14}$$

which reduces to the mobility condition proposed in [10] if $F_l = 0$, $F_a = 0$, and the point C coincides with the point O.

VI. Object Mobility Model

A. Core Dynamics

The cylindrical object with a large aspect ratio ($L >> D$) is in motion when the object burial percentage Shields parameter $\theta_{\rm opb}$ [13], [14]

$$\theta_{\rm opb}=\frac{\theta_0}{\pi}\left[\frac{1-p_b}{\sqrt{p_b\left(1-p_b\right)}}\left(1+p_B-2p_b\right)+2\gamma\right]$$
$$\theta_0\equiv\left[\frac{C_dU^2}{gD(S_o-1)}\right],\quad p_B=\frac{B}{D}$$
$$p_b=\frac{b}{D},\quad S_o=\frac{\rho_o}{\rho_w}>1 \tag{15a}$$

satisfies the condition [(B6) in Appendix B]

$$\theta_{\rm opb}>1. \tag{15b}$$

Here, θ_0 is the object's Shields parameter; p_B is the percentage burial; p_b is the relative depth of the rotation axis in sediment; and S_o is the relative object's density versus water density. The corresponding moment of momentum equation including added mass is given by

$$\begin{cases} I_A\dfrac{d\omega}{dt}=T_F-T_B, & \text{if } p_B<0.5, \theta_{\rm opb}>1\\ \omega=0, & \text{otherwise.}\end{cases} \tag{16}$$

Substitution of T_B in (B2) into (16) leads to

$$\begin{cases} I_A^*\dfrac{d\omega}{dt}=T_F-\Pi\left(\rho_o-\rho_w\right)\sqrt{b\left(D-b\right)}, & \text{if } p_B<0.5, \theta_{\rm opb}>1\\ \omega=0, & \text{otherwise}\\ I_A^*=I_A+\left(\dfrac{D}{2}-b\right)\rho_w\Pi\left(D/2+B/2-b\right)\end{cases} \tag{17}$$

with

$$I_A=I_o+\rho_o\Pi D^2/4 \tag{18}$$

where I_o is the rolling moment about the symmetric axis of the munition; I_A is the rolling moment of munition about the point b (see Fig. 9) using the parallel axis theorem; and Π is the volume of the munition.

Let the relative horizontal velocity of the rolling object be defined by

$$\hat{u}_o=\frac{u_o}{U} \tag{19}$$

which makes $\hat{u}_o$ follow the direction of U. Substitution of (3), (B1), and (B2) into (17) and use of (19) lead to a special Riccati equation

$$\begin{cases}\dfrac{d(1-\hat{u}_o)}{dt}+\alpha(1-\hat{u}_o)^2=\beta, & \text{if } p_B<0.5, \theta_{\rm opb}(t)>1\\ \hat{u}_o=0, & \text{otherwise}\end{cases} \tag{20}$$

where

$$\alpha=\frac{(1-2p_b)}{8I_A^*}\rho_wC_d\left|U\right|D^3L \times\left[\left(1-p_B\right)\left(1+p_B-2p_b\right)+2\gamma\sqrt{p_b\left(1-p_b\right)}\right]>0$$
$$\beta=\frac{(1-2p_b)}{2I_A^*\left|U\right|}g\rho_w\Pi\left(S_o-1\right)D^2\sqrt{p_b\left(1-p_b\right)}>0. \tag{21}$$

The special Riccati equation (20) integrated from t_k to t_k+1 ($k = 0, 1, 2, \ldots, K$–1) has an analytical solution [16] with α_k and β_k as known constants during the integration. Substitution of (22), shown at the bottom of the next page, into (19) leads to the dimensional horizontal velocity of the rolling object, $u_o(t) = U\hat{u}_o(t)$, which should be used for each time interval Δt. The solution (22) depends on (α_k, β_k), which involves the following three types of parameters:

1) time-independent physical parameters of the object for S_o, Π, L, and D;
2) time-dependent water velocity $U(t_k)$ from observational data or numerical modeling;
3) time-dependent relative depth of sediment rolling axis $[p_b(t_k)]$, and burial percentage $[p_B(t_k)]$ determined using a scour burial model.

Let l be the displacement of object

$$dl/dt=u_o. \tag{23}$$

Integration of l with respect to time t leads to the munition's displacement.

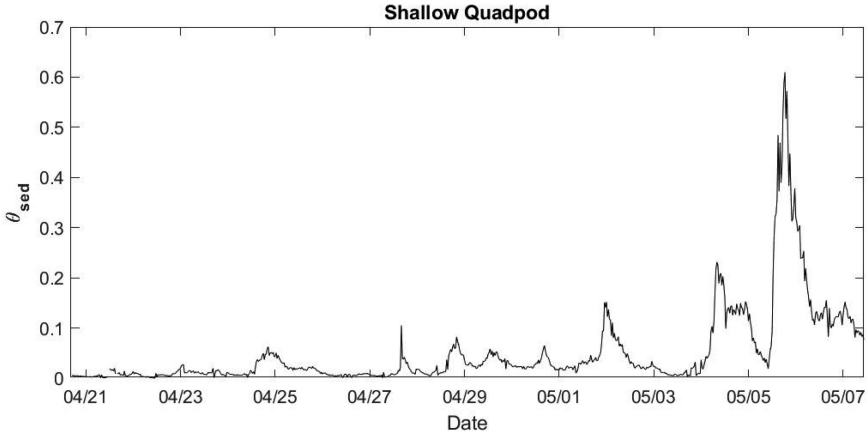

Fig. 10. Time series of sediment Shields parameter at the shallow quadpod.

VII. Scour Burial Model

Existing studies on scour burial were all concentrated on motionless objects. The ratio between the fluid force (bottom shear stress) and the weight of the sediment particles, i.e., the sediment Shields parameter ($\theta_{\rm sed}$)

$$\theta_{\rm sed} = \frac{f U_{br}^2}{g(S_{\rm sed}-1)d_{50}}, \qquad S_{\rm sed}=\frac{\rho_s}{\rho_w}$$
$$f = \exp\left[5.5\left(\frac{6U_{br}T_P}{\pi d_{50}}\right)^{-0.2} - 6.3\right] \tag{24}$$

is crucial for scour burial of motionless object and in turn for prediction of the percentage burial parameter $p_B(t) = B/D$ [12]–[14]. Here, f is the wave friction factor [17], ρ_s is the sediment grain density, and d_{50} is the median sand grain size. Using of the wave data (T_P, U_{br}) from Fig. 6(e) and (g), and sediment parameters (ρ_s, d_{50}) from (1), the sediment Shields parameter ($\theta_{\rm sed}$) are calculated from April 21 to May 23, 2013. It is less than 0.2 all the time except two atmospheric cold fronts passing by between May 4 and 6, 2013. The maximum value of $\theta_{\rm sed}$ reached 0.61 (see Fig. 10).

As pointed in [13], the equilibrium percentage burial $p_{B,\rm eq}$ for motionless cylinders induced by scour tends to increase as $\theta_{\rm sed}$ increases. An empirical formula has been established

$$p_{B,\rm eq} = a_1\theta_{\rm sed}^{a_2} - a_3 \tag{25}$$

with different choices of the coefficients (a_1, a_2, a_3) determined experimentally for cylinders subject to steady currents: $a_1 = 11$, $a_2 = 0.5$, $a_3 = 1.73$ [18], $a_1 = 0.7$, $a_2 = a_3 = 0$ [19], $a_1 = 2$, $a_2 = 0.8$, $a_3 = 0$ [20], and for cylinders under waves (depending on wave period): $a_1 = 1.6$, $a_2 = 0.85$, $a_3 = 0$ for T_p longer than 4 s [21]. For motionless cylinders before scour burial reaching equilibrium, the percentage burial follows an exponential relationship [18]

$$p_B(t_k) = p_{B,\rm eq}\left[1 - \exp\left(-\frac{t_k}{T^*}\right)\right] \tag{26}$$

where the e-folding time scale T^* is given by

$$T^* = \frac{c_1\theta_{\rm sed}^{c_2}D^2}{[g(S_{\rm sed}-1)d_{50}^3]^{0.5}}, \qquad c_1 = 1.5, c_2 = 0.11. \tag{27}$$

With the bottom wave orbital velocity (U_{br}), sediment density (ρ_s), medium grain size (d_{50}) [see (1)], and in turn the sediment Shields parameters $\theta_{\rm sed}$, the equilibrium object percentage burial $p_{B,\rm eq}$ are calculated using (25) with coefficients $a_1 = 1.6$, $a_2 = 0.85$, and $a_3 = 0$. The sediment supporting depth b (or p_b) is calculated from burial depth B (or p_B) using (11), i.e.,

$$b(t_k) = \lambda B(t_k), \qquad p_b(t_k) = b(t_k)/D = \lambda p_B(t_k)$$
$$\lambda = 0.453. \tag{28}$$

It is noted that the predicted burial percentage (p_B) computed from (25) represents the depth that an object on the surface would bury to at that moment. But an object deployed at the beginning of the time sequence would always remain buried at the deepest burial it has reached so far. The burial depth of the base of the object below the ambient seabed is equivalent to the greatest depth that the scour pit has reached up to that point in time [22]. In other words, scour only acts to bury an object deeper. It can never unbury as the time series suggested by (26). Similar to [22], we propose a simple parameterization to represent the unburial process starting from k (= 1, 2, …): 1) doing nothing if $p_B(t_{k+1}) \geq p_B(t_k)$; and 2) computing the weighted average

$$\tilde{p}_B(t_{k+1}) = wp_B(t_k) + (1-w)p_B(t_{k+1}) \tag{29}$$

$$\hat{u}_o(t) = \begin{cases} 1 - \dfrac{[1-\hat{u}_o(t_k)]\sqrt{\alpha_k\beta_k} + \beta_k \tanh\left[\left(\sqrt{\alpha_k\beta_k}\right)(t-t_k)\right]}{\sqrt{\alpha_k\beta_k} + \alpha_k[1-\hat{u}_o(t_k)]\tanh\left[\left(\sqrt{\alpha_k\beta_k}\right)(t-t_k)\right]}, \\ \quad \text{for } p_B(t_k) < 0.5, \theta_{\rm opb}(t_k) > 1 \\ 0, \quad \text{for } p_B(t_k) \geq 0.5, \theta_{\rm opb}(t_k) \leq 1, \\ \quad t_k < t \leq t_{k+1}, \alpha_k = \alpha(t_k), \beta_k = \beta(t_k) \end{cases} \tag{22}$$

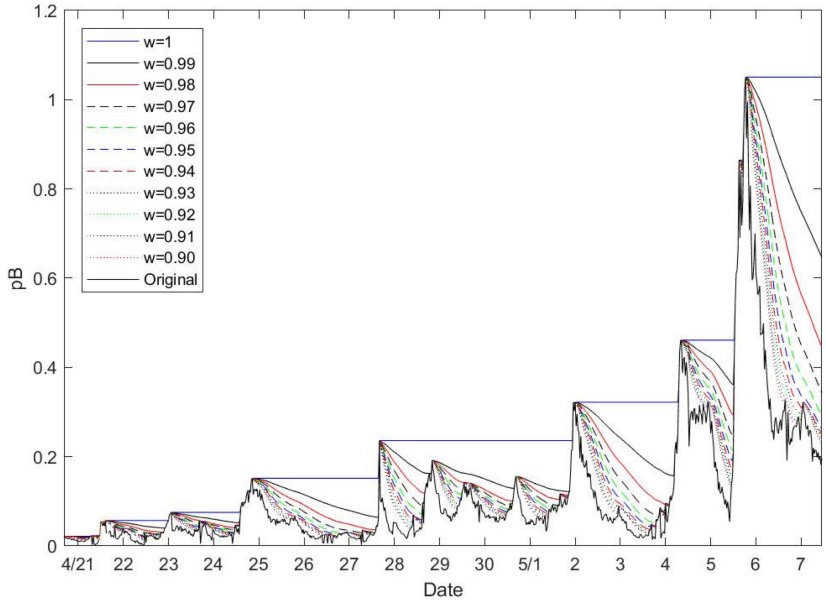

Fig. 11. Parameterization of the object's unburial with the weight coefficient varying from 0.90 to 1.00.

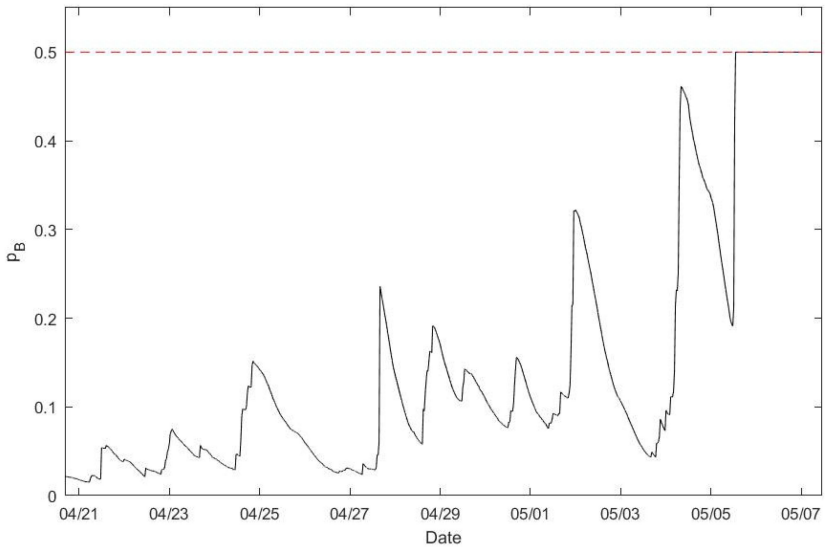

Fig. 12. Model predicted burial percentage $p_B(t)$ with unbury parameterization for each object at the shallow quadpod from April 20 to May 7, 2013. The predicted burial percentage $p_B(t)$ is less than 0.5 for all the munitions during the whole time period except during the storm event from 12:00 May 5 to 00:00 May 6, 2013.

if $p_B(t_{k+1}) < p_B(t_k)$ with w the weight coefficient. Fig. 11 shows the sensitivity of the parameterization on the weight coefficient. The stairway-type curve ($w = 1$) indicates the maximum percentage burial. For $w = 0.90$, the parameterized value $p_B(t_{k+1})$ is quite close to the original value (i.e., unparameterized). In this study, we take $w = 0.95$. The object mobility and burial models consist of (22), (23), and (25)–(29).

VIII. Prediction of Object's Mobility and Burial

Munition's mobility and burial were predicted using the object model consisting of (22), (25)–(29) with the environmental data (see Fig. 6) used as model input. The model was integrated for each surrogate (or replica) from 12:40 (14:00) local time on April 20, 2013 at shallow quadpod with its orientation shown in Fig. 4(a). For each surrogate or replica deployed in the shallow quadpod, the angle between $\mathbf{V}_w$ [data represented in Fig. 6(a), (b), and (g)] and the direction perpendicular to cylinder's main axis is determined. The velocity vector $\mathbf{V}_w$ is then transformed into $\mathbf{V}_w = (U, V)$ with U the perpendicular component, and V the paralleling component. The component U is used in the model. The object's physical parameters such as the diameter (D), volume, mass (M), and density (ρ_o) are obtained from Table I.

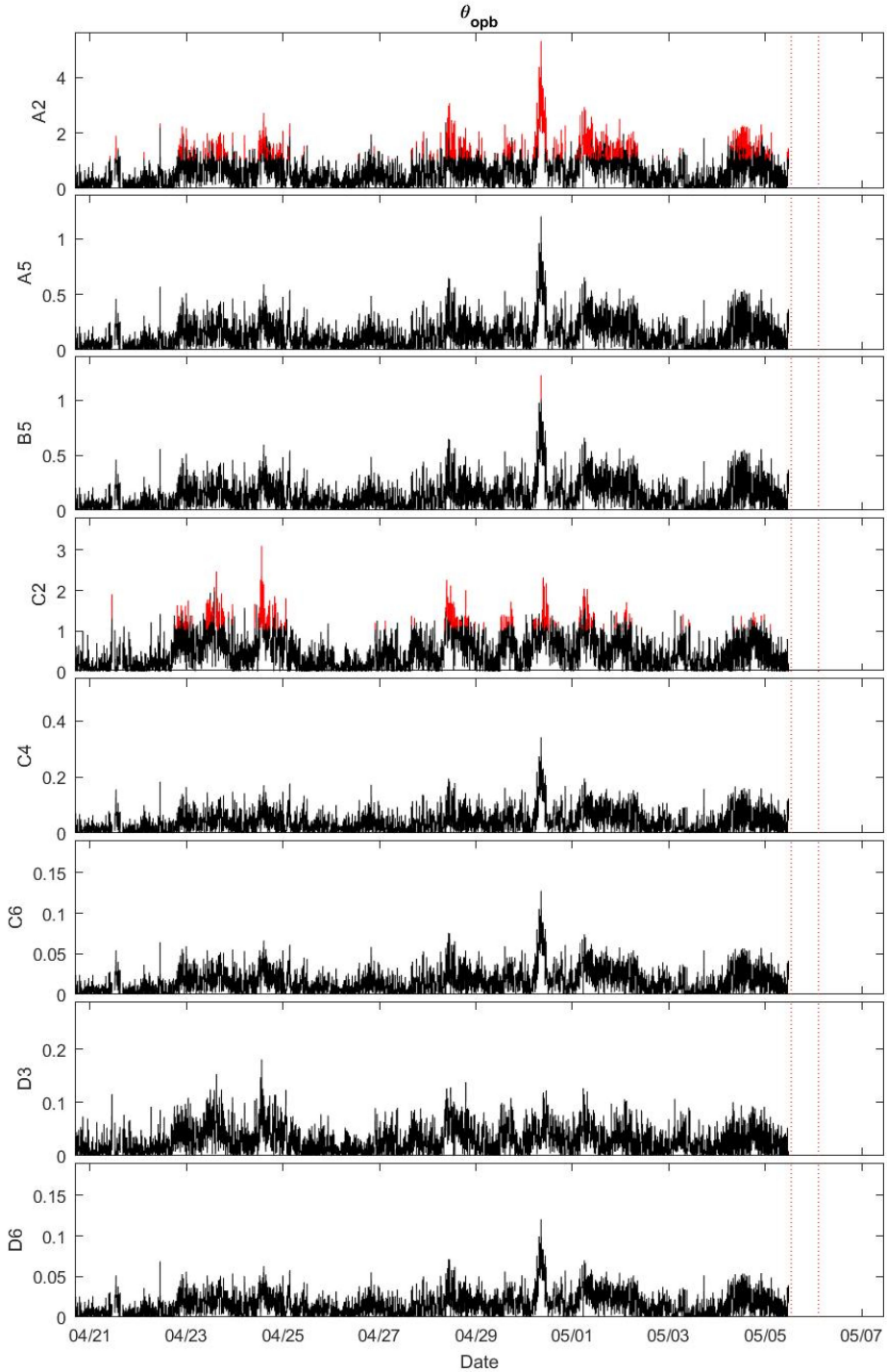

Fig. 13. Model predicted object percentage burial Shields parameters $\theta_{\rm opb}$ at the shallow quadpod from April 20 to May 7, 2013. The red color shows that the condition for rolling the object [see (19)] is satisfied. The parameter $\theta_{\rm opb}$ is not computed between 12:00 May 5 to 00:00 May 6, 2013 since the predicted burial percentage $p_B(t)$ is larger than 0.5. Among the eight objects, only A2 and C2 have evident time periods that the condition for rolling the object [see (19)] is satisfied.

The environmental data such as water depth (h), wave peak period (T_P), significant wave height (H_S), bottom wave orbital velocity (U_{br}) (shown in Fig. 6), and sediment characteristics [see (24)] are used for the scour model, i.e., (25)–(27) and (29), to get the burial percentage $p_B(t_k)$, and in turn the relative rolling center depth $p_b(t_k)$ using (28). With the object's physical parameters (D, ρ_o, M), calculated $p_b(t_k)$, and observed (or modeled) bottom current velocity component perpendicular to the cylinder's main axis $U(t_k)$, the coefficients [$\alpha(t_k)$, $\beta(t_k)$] for the object model [i.e., (22) and (23)] are calculated using (20).

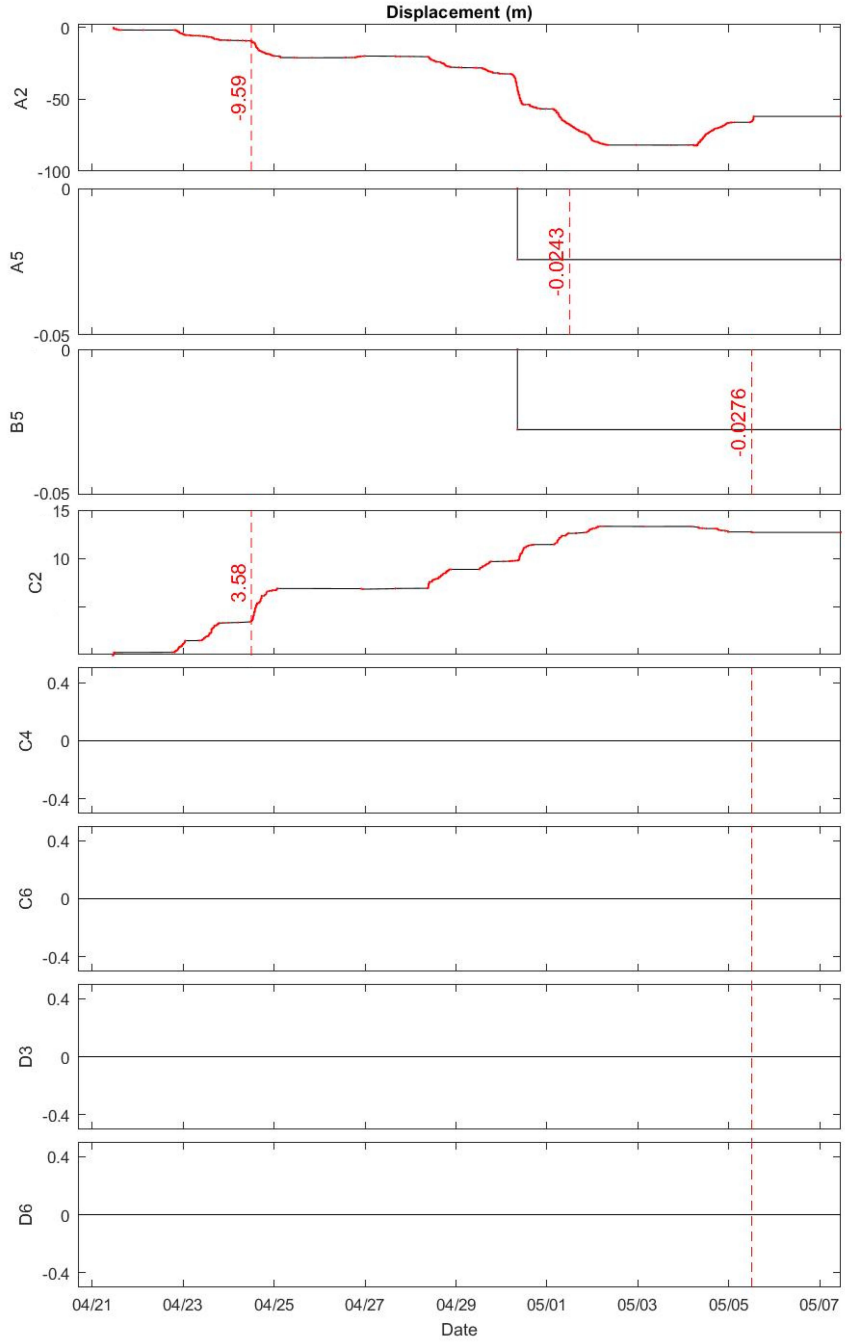

Fig. 14. Model predicted displacement $l(t)$ for each object at the shallow quadpod from April 20 to May 7, 2013. Among the eight objects, only A2 and C2 were immediately mobile and displaced 17.0 m (A2) and 6.38 m (C2) on 12:00 April 24, 2013 (dashed line); A5 and B5 were slightly mobile and displaced around 0.08 m after 12:00 April 30, 2013; C4, C6, D3, and D6 were completely motionless.

Based on the known initial locations of the objects at the shallow quadpod [see Fig. 4(a)], the model predicts the object's burial percentage [$p_B(t_k)$] with the unburial parameterization (29) shown in Fig. 12, the object percentage burial Shields parameter [$\theta_{\mathrm{opb}}(t_k)$] shown in Fig. 13, and the object's displacement [$l(t_k)$] shown in Fig. 14. The burial percentages p_B for all the objects were less than 0.5 except during the storm event on 12:00 May 5 to 00:00 May 6, 2013 local time (see Fig. 12). The red color in Fig. 13 shows that the object's rolling condition [$\theta_{\mathrm{opb}}(t) > 1$] is satisfied. Here, the two dotted lines represent the storm event.

The surrogate and replica munitions' mobility and burial were observed by divers and sector scanning sonar images during the field experiment depicted in Section II and in [9]. A total of eight munitions in place at the shallow quadpod location were recovered by divers during the maintenance dive performed on May 8, 2013 [see Fig. 4(b)]. Note that the munitions excavated by the divers at the shallow quadpod location on May 8, 2013

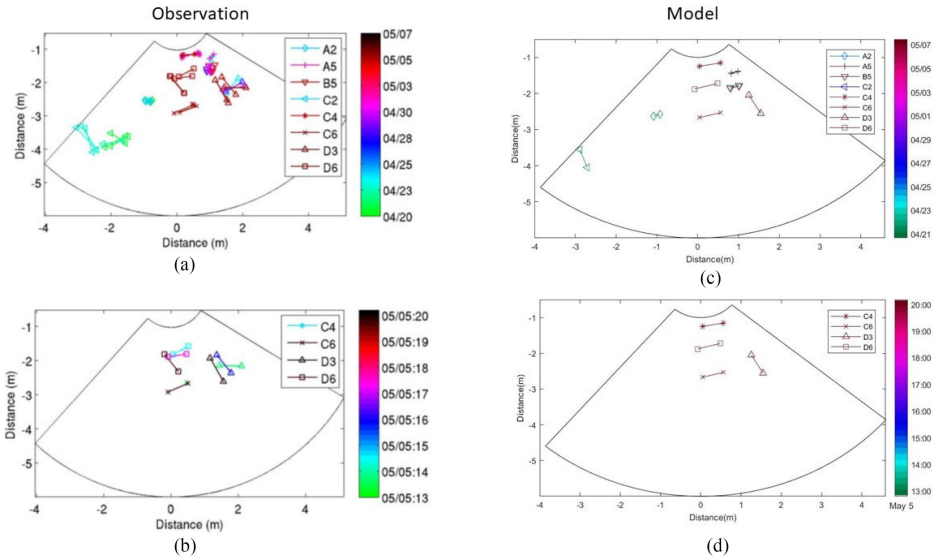

Fig. 15. Positions for all visible objects at the shallow quadpod location up to the maintenance diver performed on May 8: (a) observation for April 20–May 7, 2013; (b) observation for 13:00–20:00 on May 5, 2013; (c) model prediction for April 20–May 7, 2013; and (d) model prediction for 13:00–20:00 on May 5, 2013. Note that Fig. 15(a) and (b) was copied from [9]. The color bars denote the last time when each object was visible with dates for (a) and (c) and hour on May 5 for (b) and (d).

were immediately redeployed for the duration of the experiment. An overview of the observed munitions' mobility throughout the whole TREX13 experiment (April 20–May 7, 2013) is shown in Fig. 15(a), and during the storm event on 13:00–20:00 May 5, 2013 in Fig. 15(b). Objects A2 and C2 were immediately mobile and transported out of the field of view because they were last seen on April 23, 2013. However, the other objects were almost not mobile [see Fig. 15(a)]. The predicted objects' displacements (see Fig. 14) are consistent with the observations with large values of 9.59 m for A2 and 3.58 m for C2 on 12:00 April 24, 2012, and with near zero for the rest of the objects (see Fig. 14). Furthermore, overview of the modeled objects' mobility throughout the whole TREX13 experiment (April 20–May 7, 2013) is shown in Fig. 15(c), and during the storm event on 13:00–20:00 May 5, 2013 in Fig. 15(d). The similarity between the observation [Fig. 15(a) and (b)] and the model prediction [Fig. 15(c) and (d)] shows model capability.

However, the discrepancy between the two shows the model limitation. For example, yaw of munitions D3 and D6 was observed [Fig. 15(a) and (b)], but not predicted [Fig. 15(c) and (d)]. The munition D3 [rightmost triangles in Fig. 15(a) and (b)] moved, and then moved back; so, perhaps a net displacement of 0 m is correct, however the model predicted a value of $l = 0$ m by predicting that D3 never moved [see Figs. 14 and 15(c) and (d)]. The model limitation is due to the following four assumptions:

1) cylinder with a large aspect ratio ($L>>D$);
2) no yaw and pitch;
3) percentage burial depth less than 0.5;
4) flat seabed.

Even if the bottom profile is flat when the object is deployed, the sand tends to accumulate in front of the object and to be eroded on the opposite side thus creating a wavy bed that affects the dynamics of the object. The model will lose capability in the real world if the shape of munition is evidently different from the cylinder with $L >> D$ and the effect of wavy seabed is large on the dynamics of the object.

IX. Conclusion

The following points summarize this article.

1) A numerical model was recently developed to predict underwater cylindrical objects' mobility and burial in sandy bed, on the basis of the results from SERDP sponsored projects such as MR-2224, MR-2227, MR-2319, and MR-2320, and ONR sponsored mine burial project. The roll of the object is the major dynamics of this model with a new concept of its rolling center in the sediment. The object's displacement caused by rolling satisfies the Riccati equation with analytical solution. Along with the dynamical model, the empirical scour model [13] is used as part of the prediction system.
2) Data collected during TREX13 off the coast of Panama City, FL, USA at shallow and deep quadpods from April 21 to May 23, 2013 from the SERDP project MR-2320 were used as model input or model verification depending on the data type. The environmental data such as bottom currents, water depth (h), peak period (T_p), significant wave height (H_S), sediment density (ρ_s), and median grain size (d_{50}) are taken as input to calculate the bottom wave orbital velocity U_{br} and sediment Shields parameter θ_{sed}, and in turn the burial percentage p_B and the sediment depth percentage (p_b). The object's physical characteristics data such as diameter (D), relative density (S_o), mass (M), and rolling moment (I_o) are taken as input to the object model. The objects' positions tracked by the sector scanning sonar

images are used for model evaluation. The predicted objects' positions agree qualitatively well with the observed surrogates (or replicas) data.

3) The model developed in this study is for cylindrical object only. Also, it only considers the roll of the cylinder around its major axis. The model ignores pitch and yaw. Besides, the seabed is assumed flat. It is necessary to extend the modeling effort to more realistic seabed environment, object shapes, and more complete motion for operational use.

Appendix A
Drag and Lift Coefficients

For cylindrical objects, the drag force is decomposed into along and cross-axis components. The drag coefficient across cylinder's main axis C_d depends on the Reynolds number

$$\mathrm{Re} = \frac{UD}{\nu} \tag{A1}$$

where $\nu = 0.8 \times 10^{-6}$ m^2/s is the seawater kinematic viscosity; U is the horizontal water velocity perpendicular to the cylinder's main axis; and D is the cylinder's diameter (see Fig. 1). An empirical formula is used to calculate C_d [23]

$$C_d = \begin{cases} 1.9276 + 8/\mathrm{Re}, & \text{if Re } \le 12 \\ 1.261 + 16/\mathrm{Re}, & \text{if } 12 < \mathrm{Re} \le 180 \\ 0.855 + 89/\mathrm{Re}, & \text{if } 180 < \mathrm{Re} \le 2000 \\ 0.84 + 0.00003\mathrm{Re}, & \text{if } 2000 < \mathrm{Re} \le 12\,000 \\ 1.2 - 4/\eta & \text{if } 12\,000 < \mathrm{Re} \le 150\,000, \eta \ge 10 \\ 0.835 - 0.35/\eta, & \text{if } 12\,000 < \mathrm{Re} \le 150\,000, 2 \le \eta < 10 \\ 0.7 - 0.08/\eta, & \text{if } 12000 < \mathrm{Re} \le 150\,000, \eta < 2 \\ 1.875 - 0.0000045\mathrm{Re}, & \text{if } 150\,000 < \mathrm{Re} \le 350\,000 \\ 1/(641550/\mathrm{Re} + 1.5), & \text{if Re} > 350\,000 \end{cases} \tag{A2}$$

where $\eta = L/D$ is the cylinder's aspect ratio.

Appendix B
Threshold for Initiation of Object Migration

The drag and lift forces roll the object forward with the total torque (see Fig. 9)

$$\begin{aligned} T_F &= F_d\,(D/2 + B/2 - b) + F_l\sqrt{b\,(D-b)} \\ &= \frac{1}{2}C_d\rho_w U^2 L\left[(D-B)\,(D/2 + B/2 - b) \right. \\ &\qquad \left. + \frac{C_l}{C_d} D\sqrt{b\,(D-b)}\right]\left(1 - \frac{u_o}{U}\right)^2. \end{aligned} \tag{B1}$$

The buoyancy force and added mass roll the object backward with the torque $T_B = T_w + T_a$

$$\begin{aligned} T_B &= F_w\sqrt{b\,(D-b)} + F_a(D/2 + B/2 - b) \\ &= \frac{\pi}{4} gLD^2\,(\rho_o - \rho_w)\,\sqrt{b\,(D-b)} \\ &\quad + \frac{du_o}{dt}\rho_w \Pi(D/2 + B/2 - b). \end{aligned} \tag{B2}$$

When $T_F > T_B$, the object accelerates if it is in motion or starts to move if it is at rest ($u_o = 0$, $du_o/dt = 0$). When $T_F < T_B$, the object decelerates if it is in motion or keeps motionless if it is at rest. When $T_F = T_B$, the object keeps velocity constant if it is in motion or keeps motionless if it is at rest. Thus, the threshold for the munition's mobility becomes

$$T_F > T_B. \tag{B3}$$

The acceleration–deceleration ratio is defined by

$$\frac{T_F}{T_B} = \theta_{\mathrm{opb}}\left(1 - \frac{u_o}{U}\right)^2 \tag{B4}$$

where

$$\begin{aligned} \theta_{\mathrm{opb}} &= \frac{\theta_0}{\pi}\left[\frac{1 - p_b}{\sqrt{p_b\,(1-p_b)}}\,(1 + p_B - 2p_b) + 2\gamma\right] \\ \theta_0 &\equiv \left[\frac{C_d U^2}{gD(S_o - 1)}\right], \quad p_b = \frac{b}{D}, \quad S_o = \frac{\rho_o}{\rho_w} > 1. \end{aligned} \tag{B5}$$

Here, θ_{opb} is the object percentage burial Shields parameter based on p_b [13]; and S_o is the relative density of the object. For motionless munition ($u_o = 0$), the condition for the object to move is obtained through substituting (B4) into (B3) [10]

$$\theta_{\mathrm{opb}} > 1. \tag{B6}$$

References

[1] SERDP, "Munitions in the underwater environment: State of the science and knowledge gaps," White Paper, 2010. [Online]. Available: https://www.serdp-estcp.org/Featured-Initiatives/Munitions-Response-Initiatives/Munitions-in-the-Underwater-Environment

[2] P. Traykovski, M. D. Richardson, L. A. Mayer, and J. D. Irish, "Mine burial experiments at the Martha's Vineyard Coastal Observatory," *IEEE J. Ocean. Eng.*, vol. 32, no. 1, pp. 150–166, Jan. 2007.

[3] P. C. Chu, "Mine impact burial prediction from one to three dimensions," *Appl. Mech. Rev.*, vol. 62, no. 1, 2009, Art. no. 010802.

[4] P. C. Chu, C. W. Fan, A. D. Evans, and A. F. Gilles, "Triple coordinate transforms for prediction of falling cylinder through the water column," *J. Appl. Mech.*, vol. 71, pp. 292–298, 2004.

[5] P. C. Chu, A. F. Gilles, and C. W. Fan, "Experiment of falling cylinder through the water column," *Exp. Therm. Fluid Sci.*, vol. 29, pp. 555–568, 2005.

[6] P. C. Chu and C. W. Fan, "Pseudo-cylinder parameterization for mine impact burial prediction," *J. Fluids Eng.*, vol. 127, pp. 1515–1520, 2005.

[7] P. C. Chu and C. W. Fan, "Prediction of falling cylinder through air-water-sediment columns," *J. Appl. Mech.*, vol. 73, pp. 300–314, 2006.

[8] P. C. Chu and C. W. Fan, "Mine impact burial model (IMPACT35) verification and improvement using sediment bearing factor method," *IEEE J. Ocean. Eng.*, vol. 32, no. 1, pp. 34–48, Jan. 2007.

[9] J. Calantoni, T. Staples, and A. Sheremet, "Long time series measurements of munitions mobility in the wave-current boundary layer," Interim Rep., U.S. Strategic Environ. Res. Develop. Program, Alexandria, VA, USA, Project MR-2320, 2014.

[10] P. Traykovski and T. Austin, "Continuous monitoring of mobility, burial, and re-exposure of underwater munitions in energetic near-shore environments," Final Rep., U.S. Strategic Environ. Res. Develop. Program, Alexandria, VA, USA, Project MR-2319, 2017.

[11] C. T. Friedrichs, S. E. Rennie, and A. Brandt, "Simple parameterized models for predicting mobility, burial and re-exposure of underwater munitions," Final Rep., U.S. Strategic Environ. Res. Develop. Program, Alexandria, VA, USA, Project MR-2224, 2016.

[12] S. E. Rennie, "Underwater munitions expert system to predict mobility and burial," Final Rep., U.S. Strategic Environ. Res. Develop. Program, Alexandria, VA, USA, Project MR-2227, 2017.

[13] S. E. Rennie, A. Brandt, and C. T. Friedrichs, "Initiation of motion and scour burial of objects underwater," *Ocean Eng.*, vol. 131, pp. 282–294, 2017.
[14] C. T. Friedrichs, S. E. Rennie, and A. Brandt, "Self-burial of objects on sandy beds by scour: A synthesis of observations," in *Scour and Erosion*, J. M. Harris and R. J. S. Whitehouse, Eds. Boca Raton, FL, USA: CRC Press, 2016, pp. 179–189.
[15] P. L. Wiberg and C. R. Sherwood, "Calculating wave-generated bottom orbital velocities from surface wave parameters," *Comput. Geosci.*, vol. 34, pp. 1243–1262, 2008.
[16] E. Kamke, *Differentialgleichungen: Losungsmethoden und Losungen, I, Gewohnliche Differentialgleichungen*. Leipzig, Germany: B. G. Teubner, 1977.
[17] P. Nielsen, *Coastal Bottom Boundary Layers and Sediment Transport* (Advanced Series on Ocean Engineering), vol. 4, Singapore: World Scientific, 1992, p. 324.
[18] R. Whitehouse, *Scour at Marine Structures: A Manual for Practical Applications*. London, U.K.: Thomas Telford Publ., 1998, p. 198.
[19] B. M. Sumer, C. Truelsen, T. Sichmann, and J. Fredsøe, "Onset of scour below pipelines and self-burial," *Coastal Eng.*, vol. 42, pp. 313–335, 2001.
[20] S. T. Demir and M. H. García, "Experimental studies on burial of finite length cylinders under oscillatory flow," *J. Waterway, Port, Coastal Ocean Eng.*, vol. 133, no. 2, pp. 117–124, 2007.
[21] Y. A. Cataño-Lopera, S. T. Demir, and M. H. García, "Self-burial of short cylinders under oscillatory flows and combined waves plus current," *IEEE J. Ocean. Eng.*, vol. 32, no. 1, pp. 191–203, Jan. 2007.
[22] A. C. Trembanis *et al.*, "Predicting seabed burial of cylinders by wave-induced scour: Application to the sandy inner shelf off Florida and Massachusetts," *IEEE J. Ocean. Eng.*, vol. 32, no. 1, pp. 167–183, Jan. 2007.
[23] H. Rouse, *Fluid Mechanics for Hydraulic Engineers*, 1st ed. New York, NY, USA: McGraw-Hill, 1938, p. 422.

Peter C. Chu (Member, IEEE) received the Ph.D. degree in geophysical sciences from University of Chicago, Chicago, IL, USA, in 1985.

In 1986, he joined the Department of Oceanography, Naval Postgraduate School, Monterey, CA, USA, as an Adjunct Professor. He was promoted to Professor in 2000 and Distinguished Professor in 2011. Since 2012, he has been the Chair of the Department of Oceanography. He has authored/coauthored more than 400 papers with 200 peer-reviewed journal articles, and three books.

Dr. Chu is a Fellow of the American Meteorological Society, was the Co-Chief Editor for the *Journal of Atmospheric and Oceanic Technology* from 2009 to 2015, and has been the Chairman of the UNESCO/Intergovernment Ocean Commission Global Temperature and Salinity Profile Program since 2018.

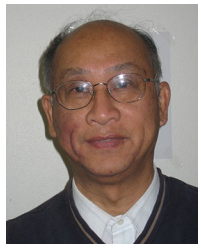

Chenwu Fan received the master's degree in mechanic engineering from China Textile University, Shanghai, China, in 1982.

He is an Oceanographer with the Naval Postgraduate School, Monterey, CA, USA. His research interests include numerical simulation, ocean analysis and prediction, coastal modeling, littoral zone oceanography for mine warfare, and mine impact burial prediction.

Joseph Calantoni (Member, IEEE) received the B.S. degree in physics from Pennsylvania State University, State College, PA, USA, in 1996, and the M.S. and Ph.D. degrees in physics from North Carolina State University, Raleigh, NC, USA, in 1999 and 2003, respectively.

From 2002 to 2004, he was a Postdoctoral Investigator with the National Research Council Research Associateship Program at the U.S. Naval Research Laboratory, Stennis Space Center (NRL-SSC), Bay Saint Louis, MS, USA. In 2004, he became a Research Physicist at NRL-SSC. From 2009 to 2021, he was a Section Head of the Sediment Dynamics Section. In 2021, he became the Branch Head of the Seafloor Sciences Branch of the Ocean Sciences Division at NRL-SSC, where he supervises a diverse team of scientists and engineers that includes civil servants, postdoctoral investigators, and other contractors. His research portfolio is broadly focused on understanding the physical, mechanical, and acoustical properties of seafloor, estuarine, and riverine sediments through a combination of mathematical and numerical modeling, detailed laboratory measurements, and field experiments with military applications in mine warfare, Naval special warfare, and the burial and mobility of UXO. He is the coauthor of more than 50 peer-reviewed publications.

Dr. Calantoni was a recipient of the 2015 Project-of-the-Year Award for Munitions Response from the Strategic Environmental Research and Development Program.

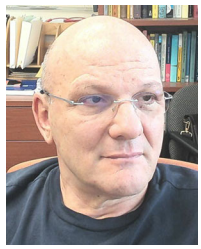

Alex Sheremet received the B.S. degree in physics from the University of Bucharest, Bucharest, Romania, in 1982, and the M.S. and D.Sc. degrees in technology from Technion, Israel Institute of Technology, Haifa, Israel, in 1993 and 1996, respectively.

He is the Michel K. Ochi Professor of Coastal Engineering with the Engineering School for Sustainable Infrastructure and Environment, University of Florida, Gainesville, FL, USA. After a postdoctoral appointment at Scripps Institution of Oceanography, University of California, San Diego, in 2001 he became an Assistant Professor with Louisiana State University. In 2005, he moved to the University of Florida, where he became an Associate Professor in 2009 and a Full Professor in 2016. He is the author of more than 60 peer-reviewed papers. His current research focuses on the nearshore transformation of ocean waves, as well as related processes, such as sediment transport, wave dissipation, and bed liquefaction.

Prof. Sheremet was a corecipient of the 2015 Strategic Environmental Research and Development Program Project-of-the-Year Award for Munitions Response, together with Dr. Calantoni.